Acta Materialia 140 (2017) 355–365

Contents lists available at ScienceDirect

Acta Materialia

journal homepage: www.elsevier.com/locate/actamat

Annealing induced void formation in epitaxial Al thin films on sapphire (α-Al_2O_3)

S.W. Hieke [a], G. Dehm [a], C. Scheu [a, b, *]

[a] Max-Planck-Institut für Eisenforschung GmbH, D-40237 Düsseldorf, Germany
[b] Materials Analytics, RWTH Aachen University, Kopernikusstr. 10, 52074 Aachen, Germany

ARTICLE INFO

Article history:
Received 14 June 2017
Received in revised form
17 August 2017
Accepted 18 August 2017
Available online 24 August 2017

Keywords:
Solid state dewetting
Thin films
Triple junction
Orientation relationship electron energy loss spectroscopy

ABSTRACT

In this work faceted voids are studied which were induced by solid state dewetting at 600 °C of tetracrystalline Al thin films covered with a native oxide layer. Hexagonally shaped voids are observed in a few locations where Al is uniformly redistributed to the surrounding thin film. Although faceted, the majority of the voids exhibit irregular shapes caused by pinning of distinct sides of the retracting Al thin film. The two different Al|void shapes (hexagonal or irregular) are investigated by site-specific cross-sectional transmission electron microscopy (TEM) analysis. The TEM studies reveal Al|void regions with and without rims and ridges. The presence of rims and ridges is explained by a discontinuous void formation process caused by pinning of the retracting Al film.

During annealing, crystallization and a thickness increase of the surface oxide, which is still continuously covering the Al thin film as well as the void, occurs. The surface scale undergoes a phase transformation from the amorphous state to γ-Al_2O_3, which is confirmed locally on the nanometer scale using scanning TEM techniques including electron energy loss near-edge structure investigations. Spherical aberration corrected atomic column resolved scanning TEM revealed a cube-on-cube orientation relationship between the Al thin film and the γ-Al_2O_3 surface oxide.

1. Introduction

Thin films are usually thermodynamically unstable in the as-deposited state due to their surface to volume aspect ratio [1,2]. Heating can lead to fragmentation of a thin film and the formation of islands, which is termed dewetting or solid state dewetting for temperatures below the melting point [1]. The process is driven by the minimization of the total energy of the system [1,3,4]. Dewetting can be beneficial for targeted nanopatterning and nanowire growth [1,5,6], especially in combination with templating techniques and has been demonstrated for various systems [7–9]. Leroy et al. reviewed recently how to control and tune solid state dewetting [10].

Miniaturization in microelectronics leads to decreasing film thicknesses in thin film devices, for which solid state dewetting is an undesired degradation process [1,4,8]. Thus, understanding the underlying mechanisms of solid state dewetting is important to suppress dewetting and prevent failure of thin film devices [1]. The process is usually described to be governed by surface self-diffusion of thin film material well below the melting temperature [8,11,12]. Hence, the addition of a capping layer is one way to suppress dewetting by surface self-diffusion [1]. The native oxide of metal thin films can prevent surface diffusion too, e.g. for Si or Al, which are well known for their passivating amorphous oxides [13]. Recent works by Kovalenko et al. [5], Amram et al. [14] and Kosinova et al. [15,16] reported the importance of grain boundary as well as interface diffusion for solid state dewetting processes.

Dewetting can start by grooving from top of the film surface or by pore formation at the substrate|film interface [1,3]. Nucleation of pores can lead to void growth towards the film surface until the complete break-up of the film is achieved [17–19]. Void growth was reported for passivated Al thin films on Si, where grain boundary diffusion was assumed as the dominating diffusion path. Thermal stresses due to cooling/heating during device operation were identified as driving forces [20–22]. Temperature induced void formation was observed in-situ by optical microscopy for Al thin films by Sugano et al. [23]. Details of the mechanism are not yet fully understood, but grain boundaries seem to be important.

---

* Corresponding author. Max-Planck Institut für Eisenforschung GmbH, Max-Planck Str. 1, 40237 Düsseldorf, Germany.

E-mail addresses: s.hieke@mpie.de (S.W. Hieke), g.dehm@mpie.de (G. Dehm), c.scheu@mpie.de (C. Scheu).

http://dx.doi.org/10.1016/j.actamat.2017.08.050

We reported recently the formation of faceted voids in a tetracrystalline Al thin film covered with a native oxide capping layer by solid state dewetting [24]. The tetracrystalline film, grown by molecular beam epitaxy, consisted of two growth variants which are both twinned. The dominating growth variant forms a heteroepitaxial orientation relationship (OR) with the single crystalline (0001) sapphire (α-Al_2O_3) substrate in accordance to literature [25,26] which will be termed *OR I a/b* in this article [24]: *OR I a/b* $\{111\} \pm <\bar{1}10>_{Al} || (0001) <10\bar{1}0>_{Al_2O_3}$ (± indicates the symmetrically equivalent twin variants *a* and *b* differing by a 180° rotation around the <111> surface normal). An additional OR was found: *OR II a/b* $\{111\} \pm <2\overline{11}>_{Al} || (0001) <10\bar{1}0>_{Al_2O_3}$. Beside void formation, annealing led to a texture evolution towards an *OR II a/b* dominated microstructure. High energy grain boundaries were identified by electron backscatter diffraction (EBSD) analysis of plan-view samples as the initial points of dewetting [24].

The appearance of the temperature induced, faceted voids led to the question which phenomena occur at the triple junctions, i.e. Al thin film|void|sapphire substrate and Al thin film|void|surface layer. The structural changes of the native oxide layer during the void formation process are also unexplored on the nanometer scale. Dutta et al. reported the presence of γ-Al_2O_3 after annealing of Al thin films using glancing X-ray diffraction on a global scale as local electron diffraction experiments were not successful [27]. The open questions will be addressed in the present work applying high resolution STEM methods including electron energy loss spectroscopy (EELS).

2. Experimental

2.1. Thin film growth and annealing treatment conditions

Details of the thin film growth can be found in Ref. [24]. In short, nominal 250 nm thick films were grown by molecular beam epitaxy (MBE, background pressure below $2 \cdot 10^{-8}$ mbar) at nominally room temperature on single crystalline (0001) oriented α-Al_2O_3 substrates. Since the deposition system setup did not allow for substrate cooling, radiation heating caused by the effusion cell led to an increase in substrate temperature up to 82 °C (measured by the thermo couple controlling the substrate heater).

Annealing treatments at 600 °C for varying times between 1 h and 45 h were carried out in a pipe furnace in Ar protective atmosphere ($p = 1.1$ bar, Ar purity: 99.999 vol%, two times purging before sample loading).

2.2. Microstructural analysis

Characterization of the as-deposited and the annealed samples was carried out by scanning electron microscopy (SEM) and EBSD using field emission gun (FEG) SEMs (a Jeol JSM 6500F and a Zeiss Merlin) or a dual beam focused-ion-beam (FIB) system (FEI Helios Nanolab 600 or 600i dual beam SEM/FIB) operated at varying accelerating voltages. The presented secondary electron micrographs were recorded either at the Zeiss SEM using an in-lens detector or at the FEI dual beam SEM/FIB using a through lens detector. In this study, SEM was used to identify voids for analysis of the interfaces as well as the triple junctions between void, Al film, oxide and substrate, respectively. Detailed plan-view studies on the evolution of grain size, Al film texture and void size were reported recently [24]. Site-specific cross-sectional specimens for transmission electron microscopy (TEM) analysis were prepared with the same FIB instruments mentioned above using the lift out technique [28]. A modified procedure of Baram et al. [29], Schaffer et al. [30] and Langford et al. [31,32] was applied. Electron beam and subsequent ion beam assisted Pt deposition (up to 2.5 μm thickness) were carried out to protect the specimen surface during Ga ion milling. 1–2 μm thick TEM lamellae were milled out of the films and transferred to a TEM grid. In general, coarse thinning at 30 kV accelerating voltage of the FIB down to a thickness of ~0.5–1 μm and subsequent fine thinning at 16 kV down to ~200 nm was used. For both, coarse and fine milling, the cleaning cross section pattern was used iteratively, whereby the beam current was varied from high (~2.8 nA) to low currents (16 pA). Final thinning of the lamellas was carried out at 5 kV (16 pA, rectangle pattern) to minimize beam damage.

TEM characterization of all films was carried out using a Jeol JEM-2200FS FEG instrument operated at 200 kV and a FEI Titan Themis 60-300 X-FEG S/TEM instrument operated at 300 kV, equipped with a probe C_s-corrector and a monochromator. The micrographs were recorded on a Gatan charge-coupled device (CCD) camera with an image size of 2 k × 2 k pixels (Jeol TEM) or a complementary metal-oxide-semiconductor (CMOS) camera with an image size of 4 k × 4 k pixels (FEI Titan). For scanning TEM (STEM) measurements a spot size of 1.5 nm (Jeol TEM) respectively 1.5 Å (Titan) was used. At the Titan Themis probe currents of ~70 pA have usually been used for imaging and 400 pA for energy-dispersive X-ray spectroscopy (EDS) measurements. Three STEM detectors were taken for imaging with the following collection semi-angle ranges: high angle annular dark field (HAADF) 73–352 mrad (except for the overview HAADF STEM micrograph in Fig. 3e, 38–189 mrad), bright field (BF) < 7 mrad and annular bright field (ABF 8–16 mrad). The convergence semi-angle has usually been 17 or 23.8 mrad. The signal of the HAADF is roughly proportional to the square of the atomic number Z [33]. EDS and electron energy loss spectroscopy (EELS) experiments were done in STEM mode using a FEI Super-X windowless EDS system with 4 synchronized silicon drift detectors and a post column (Gatan GIF Quantum ERS) energy filter, both attached to the Titan Themis.

The electron energy loss near-edge structure (ELNES) of the O-K edge (edge onset at ~532 eV [34,35]) and the Al-$L_{2/3}$ edge (edge onset at ~73 eV [34,35]) was recorded with a dispersion of 0.1 respectively 0.05 eV/channel using a semi-collection angle of 35 mrad. Due to the use of the dual EELS mode low loss data were acquired simultaneously. The full width at half maximum (FWHM) of the zero loss peak was ~0.5 eV for the chosen dispersion (FWHM at 0.01 eV/channel dispersion: ~0.27 eV). STEM-EELS mappings were acquired with subsequent addition of the spectra of individual pixels to obtain high signal to noise ratios for the Al-$L_{2/3}$ edge for the three different Al-containing materials: substrate, Al thin film and surface layer. The presented spectra were obtained by addition of 120–540 spectra at an acquisition time of 0.1 s (Al thin film, substrate) respectively 0.5 s (surface layer) acquired while scanning over an area of 36 nm by 10.8 nm (surface layer), 62 nm by 46 nm (substrate) respectively 62 nm by 21 nm (Al thin film). For O-K edge measurements the usage of the monochromator led to an insufficient signal to noise ratio, thus non-monochromated spectra were acquired with a FWHM of the zero loss peak ranging between 0.9 eV and 1.2 eV. High signal to noise ratios were obtained by addition of 5 spectra at an acquisition time of 5.0 s for the O-K edge. The pre-edge background was extrapolated using a power law function and subtracted from the original spectra [35,36].

The thicknesses of the oxide scale and the film are presented by their mean value ± standard deviation of multiple measurements. For analysis of high resolution (S)TEM micrographs, fast Fourier transforms (FFT) and diffraction patterns, the software packages EjeZ [37,38] as well as JEMS [39] were used. The Al (111) lattice fringes were taken for micrograph calibration. For the shown STEM HAADF micrographs image stacks of up to 120 images were acquired and summed up using the Smart Align software package to obtain high signal to noise ratios [40].

3. Results

3.1. Annealing induced void formation

The microstructural features induced during annealing are exemplary shown for the 6 h at 600 °C annealed sample in Fig. 1. The voids, formed during annealing of the tetracrystalline Al thin films on sapphire, are faceted and a few μm in diameter (Fig. 1a). EBSD analysis of the annealed samples confirmed that the Al grains keep the heteroepitaxial orientation relationships *OR I a/b* and *OR II a/b* with sapphire. The in-plane orientation map in Fig. 1b shows the Al grain orientations in the vicinity of a faceted void. *OR I* and *OR II* grains are both adjacent to the void which is the dominating case (82 ± 2% of the voids are in contact with *OR I* and *OR II* grains) as reported previously [24]. In addition, voids surrounded by Al grains with only *OR I* (6 ± 2%) or *II* (12 ± 2%) are also found (as shown in the overview in-plane orientation map in Supplementary Fig. 1). The faceted shape of the void is also observed in orientation maps, whereby the facets are less well resolved due to the sample tilt. The plan-view SEM micrograph in Fig. 1c shows a hexagonal shaped void with clearly defined facets, whereby short and long facets are alternating. A remaining Al feature of the retracting film is visible at one of the long facets. No rim, surrounding the void, is observed for this exemplary void which will be discussed later.

The voids can be described as inversions of Al single crystal Wulff shapes. The adjacent remaining Al film exhibits the facets originating from the anisotropy of the Al surface energy. The lowest surface energies for Al are calculated for {111}, {100} and {110} surfaces [41]. However, the calculated surface energies in literature differ a lot depending on the methodology, thus the experimentally determined averaged Al surface energy value of Kumikov et al. (1130 mJ/m^2) [42,43] was used as input value for the Wulff shape construction using the WulffMaker Mathematica code developed by Zucker et al. [44]. The Wulff shape is plotted in Fig. 1d in [111] direction and with $[\bar{1}10]$ in vertical direction as for the Al thin film marked by the white rectangle in Fig. 1c. The corresponding TEM investigation is described later. Three long sides of inclined {110} facets (yellow in Fig. 1d) and three short sides of inclined {100} facets (red) lead to the facet length alternation of the plan-view (111) facet (blue). The side facets intersect with the (111) top facet with the three directions $[\bar{1}10]$, $[01\bar{1}]$ and $[10\bar{1}]$ as indicated by the bright blue lines, arrows and captions in Fig. 1d.

3.2. Cross-sectional TEM investigations of void regions

Two different types of void shapes are found in SEM plan-view

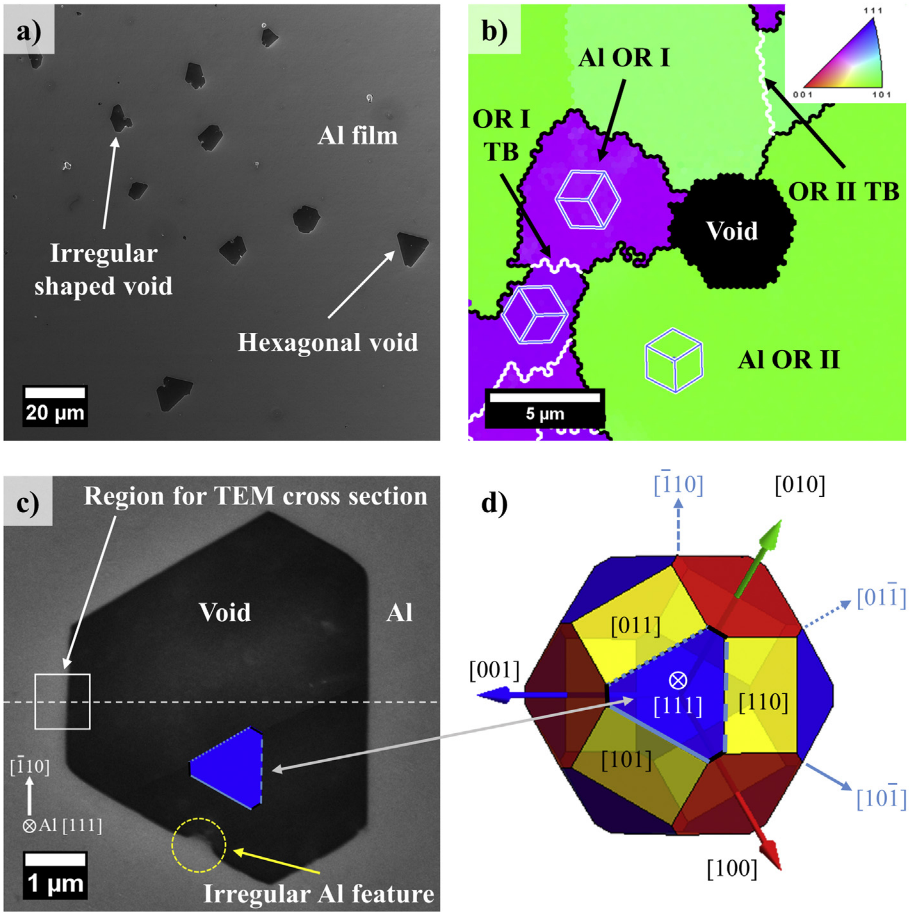

Fig. 1. a) Exemplary plan-view SEM micrograph of the sample annealed for 6 h at 600 °C containing typical microstructural features induced by solid state dewetting. b) Post annealing EBSD orientation map with cube overlays indicating the in-plane orientation of the Al thin film next to a void (*OR I* in purple, *OR II* in green, Σ3 $\{2\overline{11}\}$ twin boundaries in white, grain boundaries in black, area in black ≙ void, insert: inverse pole figure used for color coding). c) Plan-view SEM micrograph where the region for FIB sectioning and TEM analysis is marked by the dashed line. Note that the SEM micrographs a) and c) were recorded from different areas. d) Equilibrium crystal shape of a faceted Al crystal calculated with WulffMaker whereby the (111) top facet reflects the void shape in c). The lines of intersection of the (111) facet correspond to the {110} planes with the directions noted in bright blue. (For interpretation of the references to colour in this figure legend, the reader is referred to the web version of this article).

micrographs. Hexagonal voids surrounded by a homogenously thick Al film (Fig. 1c) and irregular voids surrounded by a rim are observed (Supplementary Fig. 2), the latter will be addressed later in this section. Cross sections of these regions were prepared by FIB to analyze the Al thin film|void interface as well as the triple junctions at the sapphire substrate and at the surface layer in detail.

The HAADF STEM overview micrograph in Fig. 2a shows the cross section of the Al thin film|void|substrate region marked with the white square in Fig. 1c (a low magnification HAADF STEM micrograph of the complete TEM lamella is shown in Supplementary Fig. 3a). The corresponding Al- and O-EDS mapping confirm the retraction of the Al thin film (Fig. 2b and c). The thickness of the Al layer is uniform over the lateral size of the TEM lamella in accordance to the plan-view SEM micrograph (Fig. 1c), where no rim formation at the Al|void interface was observed. Compared to the as-deposited film, the thickness increased from 242 ± 2 nm [24] to 286 ± 2 nm. The Al thin film and the void are both covered by a continuous surface oxide membrane leading to a drum-like cavity. Pt for surface protection during the FIB process growths on top of the surface oxide membrane instead of filling it as in a hole-like case.

The Al thin film|sapphire substrate interface close to the void is shown in Fig. 2d and reveal *OR I* with the close packed planes and directions parallel to each other. HAADF STEM micrographs of both triple junctions are shown in Fig. 2e and f. The distinct Al facets at the Al|void interface are assigned as (001) at the triple junction surface oxide|Al|void respectively $(\bar{1}11)$ at the triple junction substrate|Al|void and possess atomically sharp interfaces. The Wulff shape in the corresponding viewing direction confirms the identified facets. The $(\bar{1}11)$ facet is more pronounced compared to the (001) facet, which turns into a rounded shape. The Al|void interface located on the opposite site of the void in Fig. 2 was also analyzed (not shown). The Al thin film possess the same orientation relationship, whereby a well-defined $(11\bar{1})$ facet is now found on the upper part of the interface. The $(00\bar{1})$ facet on the lower part is also observed, but only for the small region close to the Al|sapphire interface and turns into a rounded shape (corresponding to the upper part of Fig. 2a). The edges at the triple junction at the surface as well as at the substrate interface are also rounded (Fig. 2e and f) which can be described as surface roughening transition.

Al- and O-EDS mappings reveal an additional aluminum oxide layer with 5 ± 1 nm thickness at the Al side wall between the Al thin film and the void (compare Supplementary Fig. 3b). No lattice fringes are observed in high resolution STEM or TEM micrographs indicating an amorphous state. A FIB artifact leading to amorphization [28] of a crystalline oxide is unlikely due to the adjacent atomic column resolved Al lattice, but cannot be excluded. On top of the side wall oxide, a non-uniform layer, containing Al, O and Ga, is observed, probably caused by redeposition during FIB milling process (Fig. 2a, b, c). Another FIB artifact is the preferential thinning of the sapphire (Fig. 2c, Supplementary Fig. 3). Defects, such as small dislocation loops, are visible in the Al film in the corresponding BF images which are most likely due to the FIB sample preparation [45,46].

Investigations of cross-sectional specimens of irregular Al|void regions by HAADF and corresponding Al- and O-EDS mappings confirm that the remaining Al thin film as well as the void are covered by a continuous oxide layer (Fig. 3a and b). On top of the oxide, a Pt layer is present resulting from the FIB sample preparation process. In contrast to the triple junction described above, a

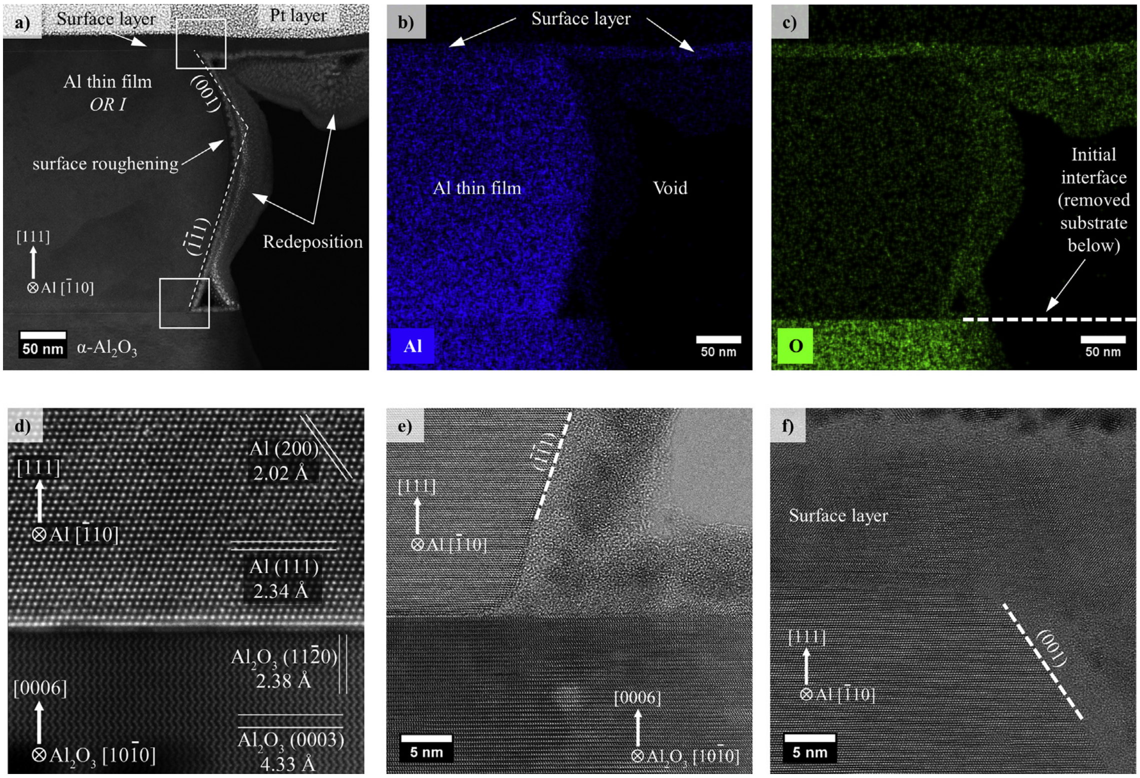

Fig. 2. a) STEM HAADF micrograph of the region marked by a rectangle in Fig. 1c of a film annealed for 6 h at 600 °C. The Al facets at the Al|void interface are indexed using the corresponding high resolution micrographs d), e) and f). b,c) Al- respectively O-EDS mappings of the region showing a continuous surface oxide layer covering the dense Al thin film as well as the void. An additional thicker Al oxide layer is found at the Al side wall at the Al|void interface and below the surface membrane. d) Spherical aberration corrected STEM HAADF micrograph of the *OR I* orientated film|substrate interface of a region close to the void taken in $[1\bar{1}0]$ Al zone axis respectively $[10\bar{1}0]$ Al_2O_3 zone axis. e,f) STEM BF micrographs showing atomically sharp facets at the triple junction of Al|void|sapphire respectively Al|void|surface layer.

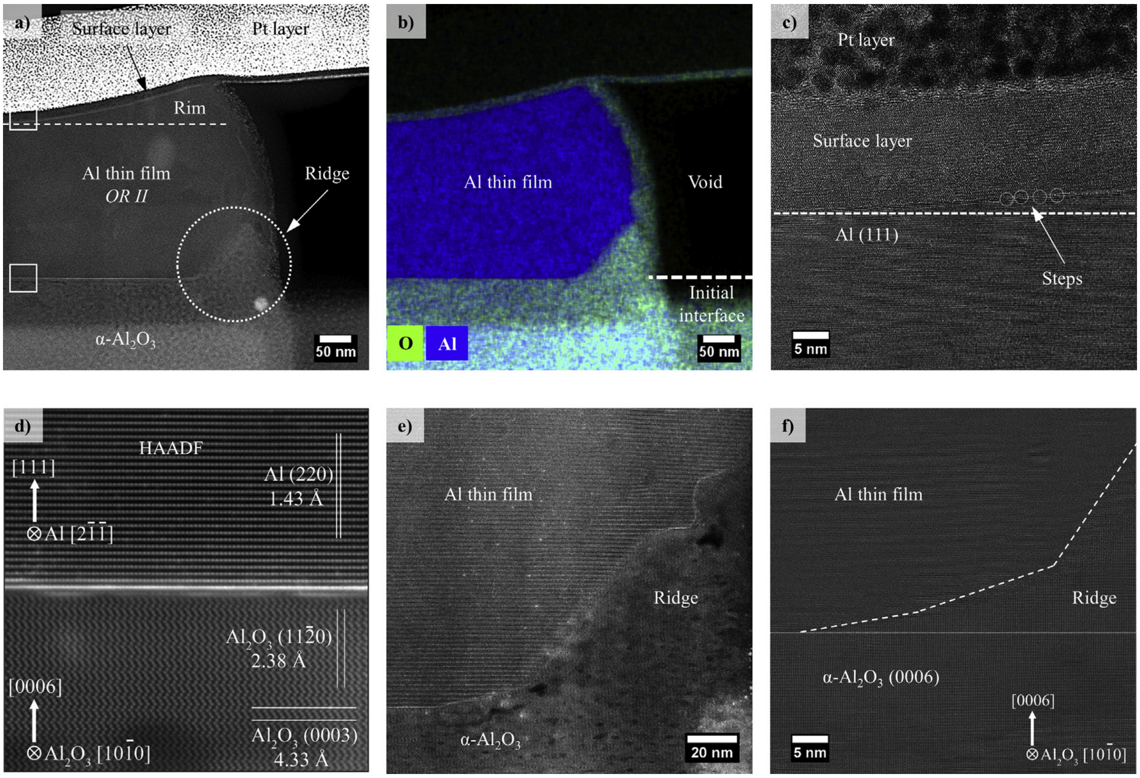

Fig. 3. a) STEM HAADF image of a rim-containing region of an Al|void interface (sample annealed at 600 °C for 1 h). b) Combined Al— and O-EDS mappings of the region indicating a faceted Al oxide ridge in addition to the Al side wall|void as well as the continuous surface Al oxide layer. c) STEM BF micrograph of the Al|surface layer interface revealing atomistic steps of the Al thin film leading to an increased film thickness towards the void (rim). d) STEM HAADF image of the OR II orientated film|substrate interface of a region close to the void taken in $[2\bar{1}\bar{1}]$ Al zone axis respectively $[10\bar{1}0]$ Al_2O_3 zone axis. e) HAADF micrograph of the ridge formed at the Al|void|substrate triple junction. f) STEM BF micrograph revealing faceted, epitaxial ridge growth continuing the sapphire substrate lattice.

ridge is found at the sapphire|Al|void triple junction. A steep rim of the Al layer at the void interface with a thickness up to ~340 nm formed. The local nature of the rim is confirmed by the thickness decrease ~400 nm away from the void down to ~250 nm which is close to the initial film thickness. At higher magnification, atomic steps towards the Al|void interface are observed at the Al|surface layer interface. A HAADF high resolution STEM micrograph of the adjacent Al thin film|sapphire substrate interface is shown in Fig. 3d and the dominating [24] orientation relationship *OR II* after annealing is identified. From the Wulff shape a {110} Al facet is expected, but the Al|void interface does not exhibit distinct facets.

In contrast to the Al|void interface faceting of the Al_2O_3 ridge is observed (Fig. 3e) at the sapphire|Al|void triple junction. A distinct assignment of the facets is not possible as the viewing direction of the Al|ridge interface ($<2\bar{1}\bar{1}>_{Al} || <10\bar{1}0>_{Al_2O_3}$) is not edge on. The ridge grows epitaxially on the α-Al_2O_3 sapphire substrate continuing the basal plane of the single crystalline sapphire substrate (see Fig. 3f). Like for the ridge-free void, an additional oxide layer with ~15–20 nm thickness between the Al thin film and the void is observed by EDS and HAADF. EDS reveals the presence of Al, O and a large amount of Ga in the outer part which is most likely redeposition due to FIB sample preparation. The sample is not viewed edge on and thus the homogenous side wall oxide is not observable. However, it can be excluded that the oxide would have completely filled the void. At the sapphire|Al film|Al sidewall oxide triple junction, lattice fringes are observed for the thin oxide between Al and the void (see Supplementary Fig. 4b). The oxide can be indexed as γ-Al_2O_3 which will be addressed in the next section.

High contrast in HAADF micrographs of FIB prepared samples at Al interfaces indicates that heavier atoms are located there (see Figs. 2d and 3d). The high contrast might be caused by an interface reconstruction [3] or Ga segregation due to FIB milling [47,48] as reported previously [24]. EDS (see Supplementary Fig. 5) and EELS measurements reveal the presence of Ga at the interface in accordance to the HAADF contrast confirming Ga artefacts of the FIB preparation process. Independent of that, an interface reconstruction might have occurred, too [3].

3.3. Phase transformation and orientation relationships of the oxide layer

A thin surface oxide layer with a thickness of 2.8 ± 0.4 nm is covering the as-deposited Al thin film as reported previously [24]. The surface scale has probably been formed after the removal of the sample from the MBE system and the first contact to atmospheric oxygen. Cross sections of samples with different annealing times were prepared by FIB to investigate the changes of the surface layer with annealing time in detail using various TEM techniques.

No lattice fringes are observed for the native oxide in the as-deposited state indicating an amorphous nature. The high resolution TEM micrograph in Fig. 4a shows the surface oxide on top of a $\Sigma 3$ twin boundary region between *OR I a* and *OR I b* which have the highest relative frequency as reported in a previous study [24]. With increasing annealing time, the thickness of the surface oxide scale is increasing from 2.8 ± 0.4 nm (as-deposited) [24], 10.7 ± 1.6 nm (1 h annealing), 13.3 ± 1.1 nm (6 h annealing) to finally 26.2 ± 3.5 nm (45 h annealing). With increasing annealing time, the surface oxide becomes less uniform and rougher as indicated by the larger scatter for the 45 h annealed sample (see Supplementary Fig. 6).

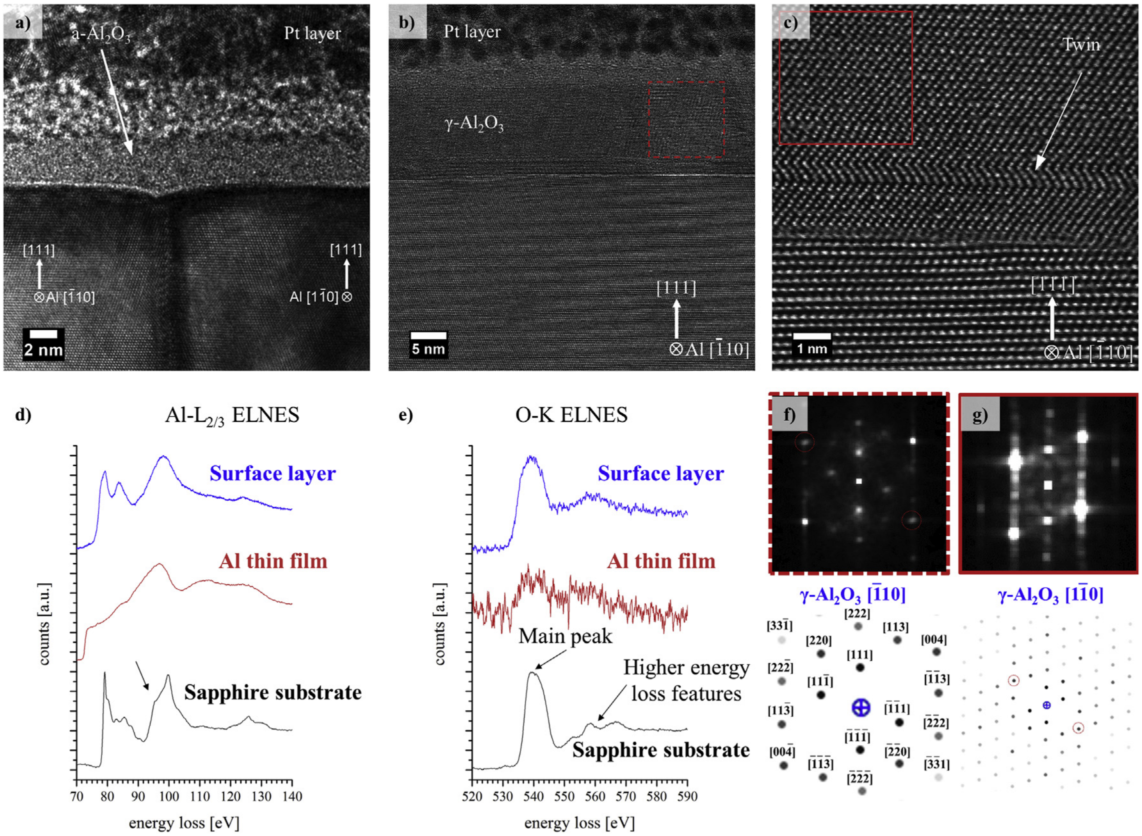

Fig. 4. a) High resolution TEM micrograph of a cross-sectional as-deposited sample indicating a continuous amorphous oxide layer covering a Σ3 twin boundary in the Al thin film. The twin boundary is observed close to edge on with the Al grains in [$\bar{1}$10] respectively [1$\bar{1}$0] zone axis. b) STEM BF micrograph revealing a crystalline surface layer covering the Al thin film after 6 h annealing. c) STEM BF micrograph of atomistic steps at the *OR I* oriented Al|surface layer interface. Nano-twinning occurs within the surface layer. d,e) Normalized EEL spectra of the Al-$L_{2,3}$ and O-K edge of the surface layer (blue spectra), the Al film (red spectra) and the sapphire substrate (black spectra). f,g) The FFTs (top) of the corresponding regions in the high resolution STEM micrographs in b) respectively c) are indexed using the diffraction patterns for γ-Al_2O_3 in ⟨110⟩ orientation (bottom, simulated pattern by JEMS). The FFTs represent the two twin variants in accordance to the twin variants of the underlying Al film present in the sample. (For interpretation of the references to colour in this figure legend, the reader is referred to the web version of this article).

The STEM HAADF micrographs in Fig. 4b and c reveal lattice fringes within the surface oxide for annealed samples indicating a phase transformation from the amorphous to the crystalline state. Local EELS measurements in STEM mode of the Al-$L_{2,3}$ and O-K edges of the different regions of the annealed samples are shown in Fig. 4d and e. Fingerprint correlation of the individual ELNES spectra [36,49] revealed the presence of three different phases: α-Al_2O_3, Al and γ-Al_2O_3. As expected, metallic Al for the thin film and α-Al_2O_3 for the substrate can be confirmed by the characteristic ELNES features: α-Al_2O_3 for the substrate exhibits an asymmetric peak at ~99 eV with an additional shoulder at ~95 eV in the Al-$L_{2,3}$ ELNES (highlighted by the arrow). The Al-$L_{2,3}$ ELNES of the surface layer shows a symmetric peak at ~99 eV and a pronounced shoulder at ~79 eV similar to EELS data reported in Refs. [36,49] indicating γ-Al_2O_3. The presence of δ-Al_2O_3 cannot be excluded since δ-Al_2O_3 is usually described as a superstructure of γ-Al_2O_3 and accordingly, the ELNES differences are expected to be small [36,50]. The O-K ELNES of the sapphire substrate shows one dominant peak at 540 eV and two characteristics peaks at ~558 eV and ~567 eV instead of one peak at ~558 eV as for amorphous, γ- or δ-Al_2O_3 [36,49]. The metallic Al layer shows a low amount of oxygen, probably due to a surface oxide of the FIB exposed side surfaces of the TEM lamella.

γ-Al_2O_3 can be described as a defect cubic spinel structure (space group F [$d\bar{3}m$]) with a fully occupied oxygen sublattice [13,51]. Al cations are distributed over the octahedral and tetrahedral sites. A refined structure, where Al ions occupy non-spinel positions, was reported in a single-crystal X-ray diffraction study [52]. The later one was used for indexing of the γ-Al_2O_3 surface layer. Fig. 4f and g show the FFTs of the regions marked in the STEM micrographs (in Fig. 4b and c) as well as the simulated diffraction patterns of the corresponding zone axis. An orientation relationship with $(111) \pm [\bar{1}10]_{Al} || (111)\ [\bar{1}10]_{\gamma-Al_2O_3}$ (OR_γ *I a*) exists between the *OR I a* oriented Al and the covering oxide. This is expected to have the lowest lattice mismatch and was found for various regions.

Within the γ-Al_2O_3 twin variants are observed. The HAADF micrograph in Fig. 4c shows the heteroepitaxial growth of the surface oxide possessing the twin variant OR_γ *I b* with $(111) \pm [\bar{1}10]_{Al} || (111)\ [1\bar{1}0]_{\gamma-Al_2O_3}$. A nanometer-wide twin in the γ-Al_2O_3 surface layer is visible close to the γ-Al_2O_3|Al interface. Due to the projection of a 3D sample, small twins embedded in the oxide layer might lead to additional {004} spots of *OR I b* in the FFT of the corresponding twin *OR I a* in Fig. 4f (marked by red circles, also in the simulated diffraction pattern in Fig. 4g). Nanometer-thin crystals are observed for different regions within the γ-Al_2O_3 layer (see Supplementary Fig. 4). Analysis of several regions indicate the presence of a second orientation relationship OR_γ *II* with $(111) \pm \left[2\bar{1}\bar{1}\right]_{Al} || (111)\ [\bar{1}10]_{\gamma-Al_2O_3}$ similar to *OR II* for Al and α-Al_2O_3. The lattice mismatches, $f_{OR\ I}$ and $f_{OR\ II}$, between the heteroepitaxial γ-Al_2O_3 surface layer and the Al thin film amount to:

$$f_{OR\ I} = \frac{d_{\gamma,440} - d_{\mathrm{Al},220}}{d_{\mathrm{Al},\,220}} = -0.020 \quad (1)$$

$$f_{OR\ II} = \frac{d_{\gamma,422} - d_{\mathrm{Al},220}}{d_{\mathrm{Al},\,220}} = 0.132 \quad (2)$$

with an Al {220}, γ-Al_2O_3 {440} and γ-Al_2O_3 {442} lattice plane spacing of $d_{Al,220} = 1.431$ Å, $d_{Al,440} = 1.403$ Å and $d_{\gamma,422} = 1.620$ Å, respectively [52,53]. The presence of a high mismatch *OR* is discussed later. To summarize, EELS and high resolution STEM images have shown that the surface layer has transformed from the amorphous state to γ-Al_2O_3 which is in accordance with literature [13,54–56].

4. Discussion

4.1. Faceted void formation

The driving force of the void formation is the reduction of the total Gibbs free energy of the system [1] by reduction of the grain boundary and the Al|substrate interface area as reported previously [24]. High energy grain boundaries involving *OR II* grains were identified as initial locations for the solid state dewetting process [24]. Void formation occurs by retraction of the Al thin film below a continuous surface oxide layer in accordance with literature reports for polycrystalline Al thin films on Si [22] as well as on sapphire [27,57]. The surface oxide is described as flexible [22,58] enough to allow void formation without rupture.

Faceting after solid state dewetting was observed for various thin film systems whereby faceting occurs for holes, for particles close to the equilibrium shape after long annealing times and at the thin film|hole interface [1,59–64]. Dutta et al. reported faceted void formation after solid state annealing of polycrystalline Al thin films on (0001) sapphire [27]. The influence and the importance of specific crystallographic orientations of the substrate respectively of the grains of the film on the dewetting mechanism were discussed in recent literature [15,16,24,61,62,65] and are confirmed in the present study involving a defined thin film containing only four *ORs*. Some voids are rotated against each other by ~30° which is in accordance to the rotation between *OR I* and *OR II* grains.

Solid state dewetting experiments by Amram et al. of Au-Fe thin films on (0001) sapphire [66] revealed the presence of faceted, hexagonal holes after annealing. Their site-specific cross-sectional TEM investigations revealed alternating {111} and {100} planes which determine the shape of the hole in the Au-Fe alloy film, similar as observed in our study. The round shape can be explained by facet roughening transitions as proposed by Burton et al. [67] due to the influence of entropy at high temperatures close to, but below the melting temperature. Above the roughening temperature facets undergo a roughening transition and become curved [68]. It is assumed that the retraction front, i.e. the Al|void interface, has a more rounded shape due to the higher impact of entropy at high temperatures and defined facets form during cooling, whereby {111} facets form faster. These observations are in accordance with literature reporting the lowest surface energy for {111} facets [41,69].

The shape of the void is determined by the mobility of the facets and can be described by the Wulff construction (Fig. 1d). The aspect ratios are reflected by an inverted Wulff shape containing the lowest energy facets which have the slowest motion. However, the aspect ratios of the short and long facets are not fully described by the idealized model as we use only an averaged experimental value for the surface energy (1130 mJ/m^2) as an input value for the Wulff construction. Small variations of the surface energies can lead to modifications in the length of the different facets. A hexagonal shape is obtained constructing a Wulff shape whereby the anisotropy of the surface energies $\gamma_{(111)}$, $\gamma_{(110)}$ and $\gamma_{(100)}$ was considered and values from first principles calculations were used [70] (see Supplementary Fig. 7). However, the calculated surface energies in literature differ a lot depending on the methodology used. $\gamma_{(111)}$ has always the lowest, but e.g. is reported in the range from 783 to 1199 mJ/m^2 [41,69,70] which changes the calculated facets in the Wulff construction strongly. Müller et al. described faceted edges in Au thin films after dewetting and also stated the importance of anisotropic surface energies [62]. Growth of hexagons with alternating short and long facets were also reported in literature for island growth of different systems, e.g. Pd islands on a bicrystalline Al_2O_3 thin film [71] or Fe on single crystalline sapphire [72].

Many of the observed voids in our study exhibit irregular or mixed faceted shapes indicating the presences of various non-equilibrium facets. We speculate that the void growth is disturbed by obstacles, i.e. steps in the substrate, grain boundaries or contamination, which is discussed in the next section. Ye et al. observed the presence of non-equilibrium facets of higher order in SEM cross sections after dewetting and hole growth in Ni (100) and Ni (110) thin films on MgO (100) and MgO (110) substrates [8]. Thus, the observed structures in our work are not in equilibrium and a frozen snapshot of the solid state dewetting process.

4.2. Al|void regions in cross section

Two different types of Al|void regions were observed in cross sections, (i) ridge-free Al|α-Al_2O_3 interfaces and (ii) those containing a rim and often a ridge. An oxide layer between the retracted Al thin film and void is observed for both types. Due to the surface layer on top of the Al film, surface diffusion is suppressed and grain boundary as well as interface diffusion were identified as important diffusion mechanisms [14,24]. The origin of O and the O diffusion processes needed for the formation of the ridge as well as of both oxide layers will be addressed later, the Al diffusion will be discussed directly.

Rim formation is often observed for solid state dewetting of thin films without passivating oxide or capping layer [14–16,62,73]. It is driven by capillary energies due to the curvature of the edge at hole|film interfaces [1]. Rim formation is usually accompanied with a valley formation behind the rim. When the bottom of a valley reaches the underlying substrate, the film can break-up and single islands might form [1,10]. Solid state dewetting without formation of an elevated rim was reported for a few thin film studies in contrast to the commonly observed rim formation [5,14,65]. Kovalenko et al. reported an increasing surface roughness as well as increasing average thickness with annealing time for Fe thin films instead of rim formation [5]. In our study, no valley formation was observed, neither for the ridge-free nor the ridge-containing Al|void regions.

Al diffusion is expected to occur along the Al|oxide interfaces. We speculate that the Al|surface layer interface is the preferred Al diffusion path as the initial amorphous as well as the vacancy-rich γ-Al_2O_3 [52] are both less dense compared to α-Al_2O_3 [74]. It is assumed that Al from the growing void region is transported to the surrounding resulting in an increased film thickness. For both Al|void|sapphire triple junction types, an increased Al film thickness is observed by SEM and TEM (see cross-sectional micrographs in Figs. 2 and 3). The Al film thickness is uniformly increased for the ridge-free type, whereas a very local increase and rim formation is observed for a ridge-containing type.

We speculate that the void formation is a discontinuous process and Al redistribution to the surrounding is highly anisotropic (see

Supplementary Fig. 2). The void, or in more specific terms distinct sides of the void, are pinned at obstacles, e.g. triple lines or steps in the substrate and the motion of the Al|void interface is stopped (see Fig. 5a). After initial void formation, the Al|void interface might act as additional, fast surface diffusion (dashed, blue arrows) path allowing circumferential diffusion at the Al side walls as well as leading to a continuing Al flux towards the Al|void|surface triple junction. Al from unpinned sites of the void accumulates at the triple line and a rim develops similar as for surface layer-free thin films during dewetting [1]. Rim formation is usually driven by the reduction of the curvature of the retracting film edge [1]. We speculate that due to the surface layer, the process only occurs in the case of pinning of the retracting Al film side wall. Due to ongoing interface diffusion (continuous, blue arrows) of Al away from the void, a curved rim with steps forms (see Figs. 3a and 5b). We assume that this process only occurs after sufficient pinning time.

The formation of a rim is also observed by Dutta et al. using cross-sectional micrographs of annealed polycrystalline Al thin films on (0001) sapphire [27]. However, the 2D scheme is an idealized model and detailed simulations are needed to investigate the mechanism in more detail. Rim formation at Al|void regions is observed for voids with well-defined facets (see Supplementary Fig. 2a) as well as for voids with irregular shapes (see Supplementary Fig. 2b). Anisotropic rim formation seems to be correlated with irregular void shapes as observed in plan-view SEM micrographs.

In addition to rim formation, sufficient pinning time may induce the formation of a sapphire ridge. Our findings reveal the presence of epitaxial α-Al_2O_3 ridges at some of the Al|void|sapphire triple junctions, despite the low temperature of 600 °C. Upon pinning, a ridge forms to compensate the unbalanced vertical component of the capillary force present at the triple phase boundary Al|void|sapphire substrate [3]. Ridge formation at triple junctions was reported in literature for various metal|Al_2O_3 systems [75–79]. Most of these studies were performed at high temperatures, e.g. sessile drop [79] or liquid dewetting experiments [78] where mass transport is sufficiently rapid [3]. It was also observed in the solid state dewetting experiments of Dutta et al. [57]. They reported epitaxial ridge formation after annealing of polycrystalline Al thin films on sapphire at 650 °C. In a subsequent study they found that the sapphire ridges formed at the periphery of faceted oxide features within Al thin films after annealing [27].

We assume that the requirement for ridge formation is sufficient time, which can be achieved due to pinning of the retracting Al film at an obstacle (e.g. surface step as in Fig. 5). The ridge prevents further retraction and may lift an existing Al rim on top. For the same annealing time, different ridge heights were observed, even for the same void at different locations. Curiotto et al. discussed the presence of ridge-free as well as ridge-containing triple phase boundaries after dewetting (both, liquid and solid) of Cu on sapphire [78,80]. Insufficient time for the receding films was reported to prevent the formation of ridges despite the unbalanced vertical forces. If pinning is overcome, the retraction of the film continues. Post annealing SEM analysis revealed the presence of ridge remains appearing as bright features (see Supplementary Fig. 8). The plan-view SEM micrograph also shows the non-uniform formation of rims surrounding the void.

An oxidized Al side wall next to the void was observed, which has a constant thickness for the rim-free Al|void regions. On top of this, a layer caused by redeposition and containing Al, O and Ga is visible. The moment when oxidation took place is not clear. It could be within the furnace (during annealing or cooling), after annealing or during the FIB sample preparation. Due to the specific facets for the rim-free sample, we speculate that the front of the retracting Al film is metallic during receding. Only during cooling, the amorphous oxide covering the Al sidewall with a thickness in the range of the native oxide is formed. For the pinned triple phase boundaries, the presence of lattice fringes in high resolution STEM micrographs indicates that the sidewall oxide forms during annealing in the furnace after sufficient pinning time (Supplementary Fig. 4b). The origin of the oxygen will be discussed in the next section.

Thus, in conclusion rim-free triple junctions form, when the film is continuously receding and Al is uniformly redistributed to the surrounding. Pinning breaks the continuous retraction and leads to irregular faceted void shapes as well as the formation of rims and ridges. Their sizes depend on the pinning time of the retracting Al film. Al rim and sapphire ridge formation are separate processes, only linked by the stopped motion of the Al|void interface, but seem to occur parallel. However, further experiments are needed to identify the microstructural features responsible for the different Al|void regions.

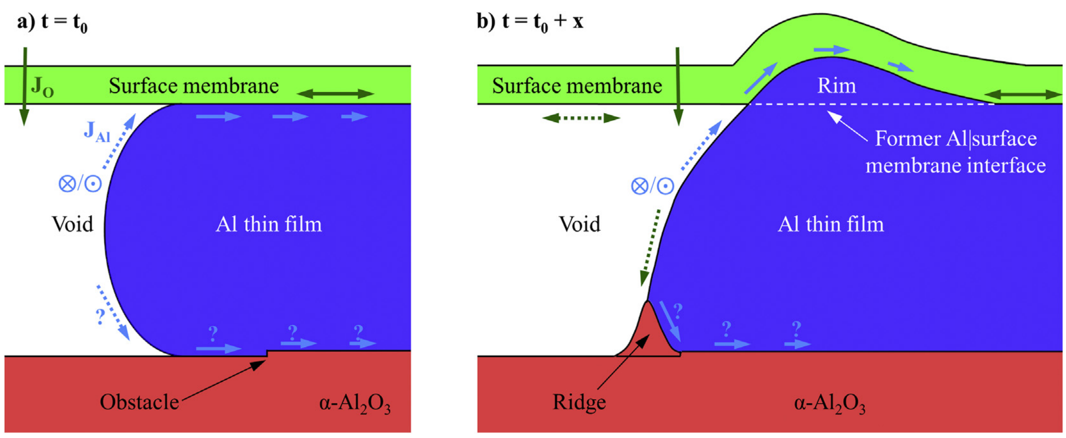

Fig. 5. Schemes of a cross-section of an Al|void region before (a) and after (b) pinning by an obstacle. The dominating mass flux is indicated by arrows (Al blue, oxygen green) whereby dashed arrows represent surface diffusion and continuous arrows represent interface (Al, oxygen) respectively volume (oxygen) diffusion, whereby surface diffusion can also occur out of plane at the Al sidewall circumferential of the void. Diffusion at the Al|sapphire interface is not expected, but cannot be excluded. Both, rim as well as ridge formation, are a consequence of the pinning of the retracting Al film sidewall. (For interpretation of the references to colour in this figure legend, the reader is referred to the web version of this article).

4.3. Surface oxide layer transformation

Dutta et al. reported the presence of γ-Al_2O_3 after annealing of Al thin films at varying temperatures between 350 °C and 650 °C using glancing X-ray diffraction on a global scale [27]. Local phase identification by electron diffraction was not successful. We showed by complementary EELS/ELNES and high resolution STEM analysis on the nanometer-scale that the surface layer of the Al thin film as well as the thin membrane above the void crystallizes from the amorphous state to γ-Al_2O_3.

The oxidation mechanism and oxide scale growth are complex and not yet fully understood [81,82]. The surface layer thickness increases with annealing time which can only occur with sufficient oxygen supply and oxygen diffusion. The presence of residual water vapor or oxygen in the Ar protective gas of the furnace might act as oxygen source. Sapphire as oxygen source is unlikely, but cannot be fully excluded. The partial pressure gradient leads to a chemical potential towards the Al thin film which can account for the oxygen inward diffusion and outward Al diffusion. The surface layer continuously covered the Al thin film as well as the voids in ex situ investigations after the annealing except rare, negligible ruptures.

Polycrystalline Al_2O_3 showed strongly temperature depending oxygen permeability under steep oxygen partial pressure gradients using grain boundary pathways for interdiffusion [83,84]. Inward diffusion of oxygen through the surface oxide was also reported for the growth of γ-Al_2O_3 crystallites below an amorphous oxide layer on Al substrates by Jeurgens et al. [13]. They reported the formation of a γ-Al_2O_3 layer up to 80 nm after annealing (500 °C, ~5.5 h, $p_{O_2} = 1.33 \cdot 10^{-4}$ Pa). Nabatame et al. and Nakamura et al. reported oxygen diffusion coefficients in amorphous and γ-Al_2O_3 layers using ^{18}O as a tracer [85,86]. The calculated diffusion length for oxygen into amorphous alumina varies depending on the temperature due to the different diffusion coefficients ($D_{587^\circ} = 4.5 \cdot 10^{-21}$ m^2/s at 587 °C [86], $D_{627^\circ} = 1.3 \cdot 10^{-20}$ m^2/s at 627 °C [86], $7.0 \cdot 10^{-20}$ m^2/s at 700 °C [85]).

For amorphous alumina, the calculated diffusion lengths are in the range of the measured oxide thickness, except for the 1 h annealed sample, which is too low (Table 1). This is different when considering γ-Al_2O_3, where reported diffusion coefficients are two or three orders of magnitudes lower than for amorphous oxide [85]. The calculated diffusion length for this case is below ~2 nm using the reported volume diffusion values ($1.8 \cdot 10^{-23}$ m^2/s at 700 °C [85]). Thus penetration of the γ-Al_2O_3 surface membrane by volume diffusion seems to be unlikely. However, Nabatame et al. commented that grain boundary coefficients are about four orders of magnitude higher compared to volume diffusion [85]. For α-Al_2O_3 enhanced grain boundary diffusion as short-circuit path is also reported by Heuer et al. who studied oxide scale growth [81,84]. As the crystalline γ-Al_2O_3 surface oxide layer on top of the Al film and the void has several grain boundaries we assume that grain boundary diffusion is taking place (Supplementary Fig. 3b).

Dutta et al. reported a surface oxide thickness of 20 ± 3 nm after 24 h annealing of Al films at 550 °C (40 ± 5 nm at 650 °C) [27]. They discussed that oxygen transport occurs via apparent fast interfacial diffusion. The homogenous thickness of the surface oxide layer in our samples indicates a fast distribution of oxygen at the Al|surface layer interface. We speculate that interfacial oxygen diffusion (continuous, green arrows in Fig. 5) is the dominating diffusion mechanism relevant for the growth of all three oxide features (surface layer, ridge, interfacial oxide at Al|void interface). Subsequent volume diffusion of oxygen through the Al thin film is unlikely due to the low solubility of oxygen in Al [27,57,87]. Al/O ion respectively Al/O vacancy diffusion at the film|surface oxide interfaces as well as at the substrate|film and at Al grain boundaries is more likely to occur [54,81]. It is assumed that the interface between film and void acts as fast oxygen surface diffusion path (dashed, green arrow in Fig. 5b) towards the film|substrate interface for ridge growth. Further experiments would be needed to determine the diffusion path.

Table 1
Comparison of calculated diffusion lengths for amorphous alumina and the measured oxide thicknesses.

Annealing time t [h]	Diffusion length [nm] (D_{587° used [86])	Diffusion length [nm] (D_{627° used [86])	Thickness of the oxide layer [nm]
1	4.0	6.8	10.7 ± 1.6
6	9.9	16.8	13.3 ± 1.1
45	27.0	45.9	26.2 ± 3.5

High resolution STEM reveals a cube-on-cube orientation relationship of two fcc materials for the γ-Al_2O_3 surface oxide on Al possessing OR_γ *I a/b* in accordance with literature [13,54–56]. The presence of *OR II*$_\gamma$ between γ-Al_2O_3 and Al is also observed (see Supplementary Fig. 4). High lattice mismatch heteroepitaxial orientation relationships are reported for different thin film systems involving metal|oxide interfaces [24,55,88]. *OR II* is unexpected considering the coincidence site lattice model, a purely geometric approach generating an idealized model describing strain. Oh et al. [88] explained the stability of *OR II* for Cu thin films on sapphire by metal-oxygen bonds. Theoretical calculations by Hashibon and Elsässer for the Cu|Al_2O_3 system revealed only slight differences in the interface energy for *OR I* and *OR II* [89]. Reichel et al. stated that ultra-thin oxide overgrowths on Al can be stabilized by a low surface energy and a high number of metal-oxygen bonds [55] which may be also the case in this study.

High resolution STEM analysis also confirmed a phase transformation to γ-Al_2O_3 of the oxide layer covering the Al side wall at the Al|sapphire ridge|void triple junction (Supplementary Fig. 4). We speculate that after formation of an amorphous oxide at the Al|void interface, a subsequent phase transformation to γ-Al_2O_3 also occurs at the triple junction. By etching of annealed Al thin films Dutta et al. [27] exposed hollow, three-dimensional oxide features which were completely surrounded by a sapphire ridge [57]. A pinned void with γ-Al_2O_3 covering the remaining Al side wall might be a primary stage of such a hollow oxide feature. Nevertheless, it cannot be excluded that the formation of oxide features within the void or Al thin film is an additional process caused by the inward diffusion of oxygen. Faceted hollow oxide features with much smaller dimensions (max. ~2 μm in diameter) grown in the void under the surface membrane were observed by SEM and TEM in FIB prepared cross sections. A detailed analysis is beyond the scope of this article.

5. Conclusion

The formation of faceted voids induced by solid state dewetting of a tetracrystalline Al thin films covered with a native oxide layer was investigated. Voids formed by the retraction of the Al thin film underneath the continuous surface oxide induced by annealing at 600 °C under Ar protective gas atmosphere.

Two different Al|void shapes were observed. In some cases, Al was redistributed isotropically to the surrounding leading to a homogenous thickness increase of the Al film and hexagonal voids with alternating short and long side facets. The ideal void shape is described by an inverse Wulff shape of Al. A faceted Al|void interface with {111} and {100} facets formed whereby surface roughening is found for the {100}/{111} facet junction as revealed by a rounded shape. Pinning of distinct sides of the retracting Al film led to a discontinuous and anisotropic retraction of the thin film and irregular void shapes. A rim formed by accumulation of Al at the Al|surface|void triple junction. Additionally, an epitaxial sapphire ridge formed as consequence of the capillary energy force component acting perpendicular to the film|substrate interface.

In both cases, the thickness of the surface oxide layer was increasing with time, whereby the layer was continuous and covered both, the Al thin film as well as the void. The details of the oxygen diffusion are not clear, but residual oxygen in the Ar atmosphere was identified as likely oxygen source. The initial amorphous surface oxide layer in the as-deposited films underwent a phase transformation to γ-Al_2O_3 after annealing. High resolution STEM and ELNES analysis of the nm-range thin oxide layer confirms γ-Al_2O_3 on a local scale. A cube-on-cube orientation relationship between Al thin film and surface oxide was observed whereby two OR containing twin variants were found.

Acknowledgement

The authors thank Gerhard Bialkowski for his assistance in thin film growth. Katja Angenendt is gratefully acknowledged for experimental and analytical support with the EBSD studies. Christian Liebscher is acknowledged for supporting STEM and EELS measurements. Helpful discussions with Gunther Richter, Eugen Rabkin, Dor Amram, Dominique Chatain, Wayne Kaplan and Uli Dahmen are highly appreciated.

Appendix A. Supplementary data

Supplementary data related to this article can be found at http://dx.doi.org/10.1016/j.actamat.2017.08.050.

References

[1] C.V. Thompson, Solid-state dewetting of thin films, Annu. Rev. Mater. Res. 42 (2012) 399–434.

[2] R.V. Zucker, G.H. Kim, W. Craig Carter, C.V. Thompson, A model for solid-state dewetting of a fully-faceted thin film, C. R. Phys. 14 (2013) 564–577.

[3] W. Kaplan, D. Chatain, P. Wynblatt, W.C. Carter, A review of wetting versus adsorption, complexions, and related phenomena: the rosetta stone of wetting, J. Mater. Sci. 48 (2013) 5681–5717.

[4] F. Niekiel, S.M. Kraschewski, P. Schweizer, B. Butz, E. Spiecker, Texture evolution and microstructural changes during solid-state dewetting: a correlative study by complementary in situ TEM techniques, Acta Mater. 115 (2016) 230–241.

[5] O. Kovalenko, J.R. Greer, E. Rabkin, Solid-state dewetting of thin iron films on sapphire substrates controlled by grain boundary diffusion, Acta Mater. 61 (2013) 3148–3156.

[6] F. Ruffino, M.G. Grimaldi, Controlled dewetting as fabrication and patterning strategy for metal nanostructures, Phys. Status Solidi (a) 212 (2015) 1662–1684.

[7] J. Ye, C.V. Thompson, Templated solid-state dewetting to controllably produce complex patterns, Adv. Mater. 23 (2011) 1567–1571.

[8] J. Ye, C.V. Thompson, Anisotropic edge retraction and hole growth during solid-state dewetting of single crystal nickel thin films, Acta Mater. 59 (2011) 582–589.

[9] F. Ruffino, M.G. Grimaldi, Self-organized patterned arrays of Au and Ag nanoparticles by thickness-dependent dewetting of template-confined films, J. Mater. Sci. 49 (2014) 5714–5729.

[10] F. Leroy, Ł. Borowik, F. Cheynis, Y. Almadori, S. Curiotto, M. Trautmann, J.C. Barbé, P. Müller, How to control solid state dewetting: a short review, Surf. Sci. Rep. 71 (2016) 391–409.

[11] D.J. Srolovitz, S.A. Safran, Capillary instabilities in thin films, I. Energ. J. Appl. Phys. 60 (1986) 247–254.

[12] D.J. Srolovitz, S.A. Safran, Capillary instabilities in thin films. II. Kinetics, J. Appl. Phys. 60 (1986) 255–260.

[13] L.P.H. Jeurgens, W.G. Sloof, F.D. Tichelaar, E.J. Mittemeijer, Structure and morphology of aluminium-oxide films formed by thermal oxidation of aluminium, Thin Solid Films 418 (2002) 89–101.

[14] D. Amram, L. Klinger, N. Gazit, H. Gluska, E. Rabkin, Grain boundary grooving in thin films revisited: the role of interface diffusion, Acta Mater. 69 (2014) 386–396.

[15] A. Kosinova, L. Klinger, O. Kovalenko, E. Rabkin, The role of grain boundary sliding in solid-state dewetting of thin polycrystalline films, Scr. Mater. 82 (2014) 33–36.

[16] A. Kosinova, O. Kovalenko, L. Klinger, E. Rabkin, Mechanisms of solid-state dewetting of thin Au films in different annealing atmospheres, Acta Mater. 83 (2015) 91–101.

[17] E. Shaffir, I. Riess, W.D. Kaplan, The mechanism of initial de-wetting and detachment of thin Au films on YSZ, Acta Mater. 57 (2009) 248–256.

[18] C.M. Müller, R. Spolenak, Dewetting of Au and AuPt alloy films: a dewetting zone model, J. Appl. Phys. 113 (2013).

[19] E. Shaffir, Y. Kauffmann, I. Riess, Void formation in gold films on yttrium-doped zirconia in the initial stage of de-wetting, Acta Mater. 79 (2014) 59–65.

[20] F.G. Yost, Voiding due to thermal stress in narrow conductor lines, Scr. Metall. 23 (1989) 1323–1328.

[21] F.G. Yost, D.E. Amos, A.D. Romig, Stress-driven diffusive voiding of aluminum conductor lines, in: 27th Annual Proceedings., International Reliability Physics Symposium, 1989, pp. 193–201.

[22] N. Kristensen, F. Ericson, J.-Å. Schweitz, U. Smith, Hole formation in thin aluminium films under controlled variation of strain and temperature, Thin Solid Films 197 (1991) 67–83.

[23] Y. Sugano, S. Minegishi, H. Sumi, M. Itabashi, In-situ observation and formation mechanism of aluminum voiding, in: 26th Annual Proceedings Reliability Physics Symposium 1988, 1988, pp. 34–38.

[24] S.W. Hieke, B. Breitbach, G. Dehm, C. Scheu, Microstructural evolution and solid state dewetting of epitaxial Al thin films on sapphire (α-Al2O3), Acta Mater. 133 (2017) 356–366.

[25] G. Dehm, B.J. Inkson, T. Wagner, Growth and microstructural stability of epitaxial Al films on (0001) α-Al2O3 substrates, Acta Mater. 50 (2002) 5021–5032.

[26] D.L. Medlin, K.F. McCarty, R.Q. Hwang, S.E. Guthrie, M.I. Baskes, Orientation relationships in heteroepitaxial aluminum films on sapphire, Thin Solid Films 299 (1997) 110–114.

[27] S. Dutta, J.M. Biser, R.P. Vinci, H.M. Chan, Solid state annealing behavior of aluminum thin films on sapphire, J. Am. Ceram. Soc. 95 (2012) 823–830.

[28] L.A. Giannuzzi, F.A. Stevie, A review of focused ion beam milling techniques for TEM specimen preparation, Micron 30 (1999) 197–204.

[29] M. Baram, W.D. Kaplan, Quantitative HRTEM analysis of FIB prepared specimens, J. Microsc. 232 (2008) 395–405.

[30] M. Schaffer, B. Schaffer, Q. Ramasse, Sample preparation for atomic-resolution STEM at low voltages by FIB, Ultramicroscopy 114 (2012) 62–71.

[31] R.M. Langford, Focused ion beams techniques for nanomaterials characterization, Microsc. Res. Tech. 69 (2006) 538–549.

[32] R.M. Langford, M. Rogers, In situ lift-out: steps to improve yield and a comparison with other FIB TEM sample preparation techniques, Micron 39 (2008) 1325–1330.

[33] S.J. Pennycook, Seeing the atoms more clearly: STEM imaging from the Crewe era to today, Ultramicroscopy 123 (2012) 28–37.

[34] C.C. Ahn, O.L. Krivanek, EELS Atlas - a Reference Guide of Electron Energy Loss Spectra Covering All Stable Elements,, ASU HREM Facility & Gatan Inc, Warrendale, PA, 1983.

[35] R.F. Egerton, Electron Energy-loss Spectroscopy in the Electron Microscope, third ed., New York Dordrecht Heidelberg London, Springer US, 2011.

[36] V. Edlmayr, T.P. Harzer, R. Hoffmann, D. Kiener, C. Scheu, C. Mitterer, Effects of thermal annealing on the microstructure of sputtered Al2O3 coatings, J. Vac. Sci. Technol. A 29 (2011), 041506.

[37] J.A. Pérez-Omil, Cádiz, Spain: Thesis of the Universidad de Cádiz, 1994.

[38] S. Bernal, F.J. Botana, J.J. Calvino, C. López-Cartes, J.A. Pérez-Omil, J.M. Rodrıguez-Izquierdo, The interpretation of HREM images of supported metal catalysts using image simulation: profile view images, Ultramicroscopy 72 (1998) 135–164.

[39] P.A. Stadelmann, JEMS - EMS Java Version, 2004. http://www.jems-saas.ch/.

[40] L. Jones, H. Yang, T.J. Pennycook, M.S.J. Marshall, S. Van Aert, N.D. Browning, M.R. Castell, P.D. Nellist, Smart Align—a new tool for robust non-rigid registration of scanning microscope data, Adv. Struct. Chem. Imaging 1 (2015) 8.

[41] L. Vitos, A.V. Ruban, H.L. Skriver, J. Kollár, The surface energy of metals, Surf. Sci. 411 (1998) 186–202.

[42] V.K. Kumikov, K.B. Khokonov, On the measurement of surface free energy and surface tension of solid metals, J. Appl. Phys. 54 (1983) 1346–1350.

[43] V.K. Kumikov, The measurement of the surface tension of some pure metals in the solid state, Mater. Sci. Eng. 60 (1983) L23–L24.

[44] R. Zucker, D. Chatain, U. Dahmen, S. Hagège, W.C. Carter, New software tools for the calculation and display of isolated and attached interfacial-energy minimizing particle shapes, J. Mater. Sci. 47 (2012) 8290–8302.

[45] P.J. Imrich, C. Kirchlechner, D. Kiener, G. Dehm, In situ TEM microcompression of single and bicrystalline samples: insights and limitations, JOM 67 (2015) 1704–1712.

[46] D. Kiener, Z. Zhang, S. Šturm, S. Cazottes, P.J. Imrich, C. Kirchlechner, G. Dehm, Advanced nanomechanics in the TEM: effects of thermal annealing on FIB prepared Cu samples, Philos. Mag. 92 (2012) 3269–3289.

[47] S. Schmidt, W. Sigle, W. Gust, M. Rühle, Gallium segregation at grain boundaries in aluminium, Z. Met. 93 (2002) 428–431.

[48] W. Hu, D.A. Molodov, B. Schönfelder, L.S. Shvindlerman, G. Gottstein, HRTEM study on $\Sigma 7$ grain boundary in aluminium bicrystals with and without Ga doping, Interface Sci. 8 (2000) 335–349.

[49] I. Levin, A. Berner, C. Scheu, H. Muellejans, D.G. Brandon, Electron energy-loss near-edge structure of alumina polymorphs, Mod. Dev. Appl. Microbeam Anal. (1998) 93–96.

[50] I. Levin, T. Gemming, D.G. Brandon, Some metastable polymorphs and transient stages of transformation in alumina, Phys. Status Solidi (a) 166 (1998)

197–218.
[51] E.J.W. Verwey, The crystal structure of γ-Fe_2O_3 and γ-$Al_{(2)}O_3$, Z. Krist. 91 (1935) 65–69.
[52] L. Smrcok, V. Langer, J. Krestan, γ-Alumina: a single-crystal X-ray diffraction study, Acta Crystallogr. Sect. C 62 (2006) i83–i84.
[53] R.W.G. Wyckoff, Crystal Structures, John Wiley & Sons, New York, London, 1963.
[54] E. Saiz, A.P. Tomsia, K. Suganuma, Wetting and strength issues at Al/α–alumina interfaces, J. Eur. Ceram. Soc. 23 (2003) 2787–2796.
[55] F. Reichel, L.P.H. Jeurgens, G. Richter, P.A. van Aken, E.J. Mittemeijer, The origin of high-mismatch orientation relationships for ultra-thin oxide overgrowths, Acta Mater. 55 (2007) 6027–6037.
[56] P.E. Doherty, R.S. Davis, Direct observation of the oxidation of aluminum single-crystal surfaces, J. Appl. Phys. 34 (1963) 619–628.
[57] S. Dutta, H.M. Chan, R.P. Vinci, Sub-surface oxidation at the aluminum–sapphire interface during low-temperature annealing, J. Am. Ceram. Soc. 90 (2007) 2571–2575.
[58] C.Y. Chang, R.W. Vook, The effect of surface aluminum oxide films on thermally induced hillock formation, Thin Solid Films 228 (1993) 205–209.
[59] F. Niekiel, P. Schweizer, S.M. Kraschewski, B. Butz, E. Spiecker, The process of solid-state dewetting of Au thin films studied by in situ scanning transmission electron microscopy, Acta Mater. 90 (2015) 118–132.
[60] P.D. Nsimama, A. Herz, D. Wang, P. Schaaf, Influence of the substrate on the morphological evolution of gold thin films during solid-state dewetting, Appl. Surf. Sci. 388 (2016) 475–482. Part A.
[61] G. Atiya, D. Chatain, V. Mikhelashvili, G. Eisenstein, W.D. Kaplan, The role of abnormal grain growth on solid-state dewetting kinetics, Acta Mater. 81 (2014) 304–314.
[62] C.M. Müller, R. Spolenak, Microstructure evolution during dewetting in thin Au films, Acta Mater. 58 (2010) 6035–6045.
[63] D. Amram, E. Rabkin, Phase transformations in Au-Fe particles and thin films: size effects at the micro- and nano-scales, JOM 68 (2016) 1335–1342.
[64] D. Chatain, S. Curiotto, P. Wynblatt, H. Meltzman, W.D. Kaplan, G.S. Rohrer, Orientation relationships of copper crystals on sapphire (10-10) m-plane and (10-12) r-plane substrates, J. Cryst. Growth 418 (2015) 57–63.
[65] P. Jacquet, R. Podor, J. Ravaux, J. Teisseire, I. Gozhyk, J. Jupille, R. Lazzari, Grain growth: the key to understand solid-state dewetting of silver thin films, Scr. Mater. 115 (2016) 128–132.
[66] D. Amram, L. Klinger, E. Rabkin, Anisotropic hole growth during solid-state dewetting of single-crystal Au–Fe thin films, Acta Mater. 60 (2012) 3047–3056.
[67] W.K. Burton, N. Cabrera, F.C. Frank, The growth of crystals and the equilibrium structure of their surfaces, Phil Trans. R. Soc. Lond. Ser. A Math. Phys. Sci. 243 (1951) 299–358.
[68] J.C. Heyraud, J.J. Métois, Growth shapes of metallic crystals and roughening transition, J. Cryst. Growth 82 (1987) 269–273.
[69] R. Li, Y. Zhong, C. Huang, X. Tao, Y. Ouyang, Surface energy and surface self-diffusion of Al calculated by embedded atom method, Phys. B Condens. Matter 422 (2013) 51–55.
[70] J. Schöchlin, K.P. Bohnen, K.M. Ho, Structure and dynamics at the Al(111)-surface, Surf. Sci. 324 (1995) 113–121.
[71] K.H. Hansen, T. Worren, S. Stempel, E. Lægsgaard, M. Bäumer, H.J. Freund, F. Besenbacher, I. Stensgaard, Palladium nanocrystals on Al2O3: structure and adhesion energy, Phys. Rev. Lett. 83 (1999) 4120–4123.
[72] D. Amram, O. Kovalenko, E. Rabkin, The $\alpha \leftrightarrow \gamma$ transformation in Fe and Fe–Au thin films, micro- and nanoparticles – an in situ study, Acta Mater. 98 (2015) 9.
[73] L. Klinger, D. Amram, E. Rabkin, Kinetics of a retracting solid film edge: the case of high surface anisotropy, Scr. Mater. 64 (2011) 962–965.
[74] I. Levin, D. Brandon, Metastable alumina polymorphs: crystal structures and transition sequences, J. Am. Ceram. Soc. 81 (1998) 1995–2012.
[75] E. Saiz, A.P. Tomsia, R.M. Cannon, Ridging effects on wetting and spreading of liquids on solids, Acta Mater. 46 (1998) 2349–2361.
[76] E. Saiz, R.M. Cannon, A.P. Tomsia, High-temperature wetting and the work of adhesion in metal/oxide systems, Annu. Rev. Mater. Res. 38 (2008) 197–226.
[77] E. Saiz, R.M. Cannon, A.P. Tomsia, Energetics and atomic transport at liquid metal/Al_2O_3 interfaces, Acta Mater. 47 (1999) 4209–4220.
[78] S. Curiotto, H. Chien, H. Meltzman, S. Labat, P. Wynblatt, G. Rohrer, W. Kaplan, D. Chatain, Copper crystals on the (11-20) sapphire plane: orientation relationships, triple line ridges and interface shape equilibrium, J. Mater. Sci. 48 (2013) 3013–3026.
[79] E. Saiz, A.P. Tomsia, R.M. Cannon, Triple line ridging and attachment in high-temperature wetting, Scr. Mater 44 (2001) 159–164.
[80] S. Curiotto, H. Chien, H. Meltzman, P. Wynblatt, G.S. Rohrer, W.D. Kaplan, D. Chatain, Orientation relationships of copper crystals on c-plane sapphire, Acta Mater. 59 (2011) 5320–5331.
[81] A.H. Heuer, D.B. Hovis, J.L. Smialek, B. Gleeson, Alumina scale formation: a new perspective, J. Am. Ceram. Soc. 94 (2011) 146–153.
[82] A.H. Heuer, Oxygen and aluminum diffusion in α-Al_2O_3: how much do we really understand? J. Eur. Ceram. Soc. 28 (2008) 1495–1507.
[83] M. Wada, T. Matsudaira, S. Kitaoka, Mutual grain-boundary transport of aluminum and oxygen in polycrystalline Al2O3 under oxygen potential gradients at high temperatures, J. Ceram. Soc. Jpn. 119 (2011) 832–839.
[84] A.H. Heuer, T. Nakagawa, M.Z. Azar, D.B. Hovis, J.L. Smialek, B. Gleeson, N.D.M. Hine, H. Guhl, H.S. Lee, P. Tangney, W.M.C. Foulkes, M.W. Finnis, On the growth of Al_2O_3 scales, Acta Mater. 61 (2013) 6670–6683.
[85] T. Nabatame, T. Yasuda, M. Nishizawa, M. Ikeda, T. Horikawa, A. Toriumi, Comparative studies on oxygen diffusion coefficients for amorphous and γ-Al_2O_3 films using 18 O isotope, Jpn. J. Appl. Phys. 42 (2003) 7205.
[86] R. Nakamura, T. Toda, S. Tsukui, M. Tane, M. Ishimaru, T. Suzuki, H. Nakajima, Diffusion of oxygen in amorphous Al_2O_3, Ta_2O_5, and Nb_2O_5, J. Appl. Phys. 116 (2014), 033504.
[87] G. Levi, W.D. Kaplan, Oxygen induced interfacial phenomena during wetting of alumina by liquid aluminium, Acta Mater. 50 (2002) 75–88.
[88] S.H. Oh, C. Scheu, T. Wagner, M. Ruhle, Control of bonding and epitaxy at copper/sapphire interface, Appl. Phys. Lett. 91 (2007) 141912–141913.
[89] A. Hashibon, C. Elsässer, M. Rühle, Structure at abrupt copper–alumina interfaces: an ab initio study, Acta Mater. 53 (2005) 5323–5332.
[90] S. Preibisch, S. Saalfeld, P. Tomancak, Globally optimal stitching of tiled 3D microscopic image acquisitions, Bioinformatics 25 (2009) 1463–1465.